J. Indian Inst Sci., July–Aug. 1999, **79**, 313–345.

IISc THESES ABSTRACTS

Thesis Abstract (Ph. D.)

Interactions of a 14 kDa β-galactoside binding animal lectin with its ligands and its role in cell-matrix adhesion by V. Radha
Research supervisor: Prof. S. K. Poddar
Department: Biochemistry

1. Introduction

Galectins are a family of β-galactoside-binding animal lectins. Those proteins which bind to β-galactoside sugars, and have considerable homology in their carbohydrate-binding domains are classified as galectins. They have been further subclassified as galectin-1, -2, etc. depending upon their molecular weights and sequence identity.[1] Galectin-1 is the protein of our interest. It is a dimer with a subunit molecular weight of 14 kDa.

Galectin-1 has all the typical characteristics of a cytosolic protein.[2] The implicated functions of this protein include roles in immune modulations,[3, 4] cell-growth inhibition,[5] cell–matrix interactions[6] and apoptosis.[7] To mediate these functions galectin has to be present in the extracellular environment. Indeed, externalization of galectin-1 by a novel secretory mechanism has been shown in muscle cells by Cooper *et al.*[8]

To mediate its implicated functions, galectin once in the extracellular environment binds to carbohydrate structures. Though qualitative studies have been done on the sugar-binding specificity of galectin-1, quantitative studies have not been carried out. Detailed analyses of the cell-binding specificity have also not been carried out. The first step towards understanding better the functions of the protein would be to understand the nature of its interactions with its ligands. One of the major implicated functions of galectin-1 is its role in cell–matrix interactions. It has been shown by many researchers that galectin-1 mediates this function by binding to one of the important extracellular matrix glycoprotein, laminin. Depending upon the cell type, galectin-1 has been shown to either promote or inhibit laminin-mediated cell adhesion.[6, 9] However, the molecular mechanism by which galectin brings about the same is not clearly understood. Considering these facts we have attempted to answer the following questions: What is the nature and specificity of interaction of galectin-1 to simple sugar ligands, and how does this compare in its interactions with complex ligands like cell-surface receptors? What is the mechanism of trimolecular interaction between galectin-1, its specific cell surface receptors(s) and laminin? What is the nature of endogenous receptors of galectin on the spleen cell surface?

2. Experimental and discussion

To achieve these objectives, we have purified and characterized a 14-kDa galectin (L-14) from sheep spleen. We have for the first time reported affinity and thermodynamic parameters for

the binding of L-14 to simple sugars.[10] The single-site binding constants of various sugars for the lectin are observed in the following order: N-acetyllactosamine > thiodigalactoside > lactose > methyl-α-galactose > methyl-β-galactose. Reactions were essentially enthalpically driven with the binding enthalpies ranging from –53.8 kJ/mol for thiodigalactoside at 301 K to –2.2 kJ/mol for galactose at 300 K indicating that hydrogen bonding and van der Waals interactions provide major stabilization for these reactions. The binding of L-14 to splenocytes shows that there are two classes of binding sites on the cells for the lectin. A high-affinity site with a K_a ranging from 1.1×10^6 to 5.1×10^5 M^{-1} and a low-affinity binding site with a K_a ranging from 7.7×10^4 to 3.4×10^4 m^{-1}. The number of receptors per cell for the high- and low-affinity sites are $9 (\pm 3) \times 10^6$ and $2.5 (\pm 0.5) \times 10^6$, respectively. The temperature dependence of the K value yielded the thermodynamic parameters. The energetics of this interaction shows that though this interaction is essentially enthalpically driven ($\Delta H - 21$kJ/mol) for the high-affinity sites, there is a very favorable entropy contribution to the free energy of this interaction ($-T\Delta S$ –17.5 kJ/mol) suggesting that hydrophobic interactions may be playing a role in this interaction. To check the specificity of binding between L-14 and splenocytes, the binding was carried out in the presence of lactose. The observed inhibition of binding was only 20%, whereas the glycoprotein asialofetuin brought about a 75% inhibition, suggesting that complex carbohydrate structures are involved in the binding of L-14 to splenocytes. To gain insight into one of the major implicated functions of L-14, namely, its role in cell–matrix adhesion, the effect of laminin on the binding of L-14 to splenocytes has been studied. Laminin enhanced the binding of L-14 to splenocytes by about 400%. L-14 also mediated the adhesion of splenocytes to laminin. Laminin alone was unable to bind to splenocytes or to promote adhesion. L-14 is a dimeric molecule and our data suggest that the dimeric lectin brings about enhanced binding and adhesion of splenocytes to the extracellular matrix glycoprotein laminin, by acting as a bridge between a laminin-L-14 complex and the splenocytes. Our studies suggest a role for L-14 in cell–matrix interactions. It is of interest, therefore, to find out the nature of endogenous ligands on splenocytes for L-14, through the binding of which L-14 could mediate its functions. There are five proteins in the membrane fraction of sheep spleen cells that bind to an L-14-Sepharose 4B column and the molecular weights of these proteins range from 55 to 272 kDa. Carbohydrate staining shows that two of these proteins range from 55 to 275 kDa. Carbohydrate staining shows that two of these proteins of molecular weights 275 and 55 kDa are glycosylated proteins. The specificity of the isolated proteins was checked by a ligand blot, where the proteins of mol. wt. 275, 170 and 78 kDa were specifically bound to L-14. These results indicate that more than one kind of protein on the surface of splenocytes bind to L-14 showing the heterogeneous nature of receptors for L-14.

References

1. BARONDES, S. H. *et al.* — *Cell*, 1994, **76**, 597.
2. KASAI, K. AND HIRABAYASHI, J. — *Biochem. J.*, 1996, **119**, 1–8.
3. PITTS, M. J. AND YANG, D. C. H. — *Biochem. J.*, 1981, **195**, 435–439.
4. LIPSICK, J. S., BEYER, E. C., BARONDES, S. H. AND KALPAN, N. O. — *Biochem. Biophys. Res. Commun.*, 1980, **97**, 56–61.

5. WELLS, V. AND MALLUCCI, L. *Cells*, 1991, **64**, 91–97.
6. ZHOU, Q AND CUMMINGS, R. D. *Arch. Biochem. Biophys.*, 1993, **300**, 6–17.
7. PERILLO, N. L., PACE, K. E. AND SEIHAMER, J. J. *Nature*, 1995, **378**, 736–739
8. COPPER, D N. W. AND BARONDES, S. H. *J. Cell Biol.*, 1990, **110**, 1681–1691.
9. COPPER, D. N. W., MASSA, S. M. AND BARONDES, S. H. *J. Cell Biol.*, 1991, **115**, 1437–1448.
10. RAMKUMAR, R., SUROLIA, A. AND PODDAR, S. K. *Biochem. J.*, 1995, **308**, 237–241.

Thesis Abstract (Ph.D.)

Numeric protection relays—multiprocessor-based hardware and software schemes by G. N. Rathna

Research supervisors: Profs K. Parthasarathy, V. Rajaraman and S. K. Nandy
Department: Electrical Engineering

1. Introduction

Protective devices are an integral part of power systems. Protective relaying community is striving to meet the demand of modern high-voltage and extra high-voltage (EHV) systems. Developments in protection techniques should keep pace with the developments in primary system so as to provide reliable and high-speed clearance of faults. Being an important integral part of the power system, the protection system should not only be reliable, sensitive and selective but also accurate and fast. Further, as the power system grows in size and complexity, protection techniques and the hardware employed for realizing the protection functions should be constantly updated to achieve higher functional reliability. Factors such as size, cost and power consumption of recent processors have come down drastically and the speed of computation has considerably increased in recent years. Multiprocessor-based hardware platforms have opened up scope for developing advanced numeric relays. This work addresses issues concerning the development of high-performance hardware schemes for numeric relay designs. The multiprocessor architecture proposed performs various numeric relaying functions such as digital filtering, numeric relaying algorithms, relay settings, relay logic, digital input/output (I/O) and other control operations to synchronize the operations of distributed processors. Based on the proposed multiprocessor architecture,[1] comprehensive integrated protection schemes for railway traction systems have been developed. The proposed architecture is extended for developing a multizone polyphase parallelogram distance relay along with accurate fault-locating algorithms for transmission lines. An integrated protection scheme for protection of AC motors has also been developed.

2. Evaluation of power-system algorithms

A detailed evaluation of significant signal-processing algorithms for power system protection has been carried out under simulated conditions of transient test data. The data (waveforms)

are computed using electromagnetic transient package (EMTP) for various line lengths and fault conditions. The transient signals generated from EMTP represent near-realistic conditions to which numeric relay would be subjected to in the field. The signals are bandlimited by an anti-aliasing filter prior to sampling. Digital filters are used to filter the harmonics in the sampled data and higher sampling rates (of the order of 5 kHz) are used to minimize the delay in digital filtering. Digital filters have advantages of precision, time invariance, flexibility and shorter group delay. The software-based implementation of digital filters considered in this work, viz. infinite impulse response (IIR) and finite impulse response (FIR) have opened scope for improving the performance of digital relaying algorithms. Based on critical evaluation of various algorithms, it is seen that differential algorithm has fast and accurate convergence to the fault value, whereas the mean square error minimization algorithm introduces least errors for saturated signals and also has faster tripping time during severe short-circuit conditions. Thus, these two algorithms in parallel enhance the reliability of the numeric relay. This work discusses the implementation of the above two algorithms in parallel which ensures fault detec-

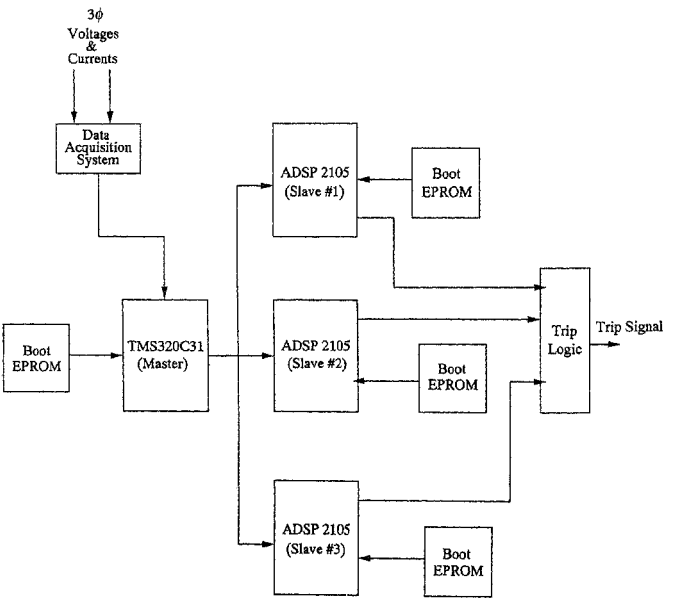

FIG. 1. Multiprocessor architecture using DSP processors.

tion within a cycle, comprising filter delay, computation of the algorithm and consistency check of the fault for three samples.

The parallel architecture proposed for numeric protection comprises four processors in master–slave configuration (Fig. 1). The front-end master processor performs IIR/FIR digital filtering using the sampled data available after signal conditioning. The master processor also coordinates the overall supervisory operations. For integrated protection, two of the slave processors run the numeric relaying algorithms in parallel and the other slave processor runs the relay logic. The proposed multiprocessor architecture has been realized using DSP and transputer-based hardware schemes.

A comprehensive numeric protection scheme for 25-kV ac railway traction application has been evaluated on the proposed hardware schemes. This provides single-phase distance protection, detection of wrong phase coupling, power transformer (PT) fuse-failure detection, differential protection for traction feeder transformer, backup over current protection for the feeder transformer as well as 25-kV overhead lines, second harmonic restraint and ΔI feature to selectively discriminate the fault current during high-resistance faults. The protection also blocks the relay operation during overload conditions. The relaying software also supports high-set instantaneous tripping against large fault currents during close-in faults. The algorithms have been developed for implementing two types of relay characteristics with multizone features, viz. one having parallelogram characteristic and the other circular mho and offset mho-type characteristics for distance protection.

For implementing polyphase distance-relaying schemes, which have high-speed computational requirement, one of the slave processors computes phase-to-phase fault while another slave processor computes phase-to-ground fault. The third slave processor performs directional measurement and fault-location functions. The numeric relaying algorithms is capable of detecting phase-to-phase faults and phase-to-ground faults. The algorithm also functions as a fault locator. Negative sequence current is used to detect open conductor situation in a transmission line or to detect any unbalanced fault occurring during a power swing blocking.[2] A multizone relay with parallelogram characteristic is used for distance protection. The reach along R and X axis can be independently set depending upon the system operating conditions. Four zones of protection are provided. Zones-1 and -2 have directional parallelogram characteristics while Zone-3 provides back-up protection for nearby reverse faults (non-directional). Zone-4 is for power-swing detection and blocking. This relay is found to ensure fault detection within a cycle for Zone-1 faults. Fault-locating algorithms based on Eriksson's method[3] and Zamora's method[4] are considered for evaluation. The Eriksson's method uses the sending end-fault currents, prefault voltages, currents and equivalent source impedances. Zamora's method uses both sending and receiving end faults, prefault voltages to detect the fault location. This approach is independent of fault currents, prefault currents, fault type, and fault resistance. Based on Eriksson's approach, the algorithm has been extended to consider all the parallel power corridors across the line under consideration.

An integrated scheme for three-phase induction and synchronous motor protection have been proposed on multiprocessor-based hardware schemes. The relaying algorithm performs the protection functions such as overvoltage, undervoltage, overload, unbalanced load, prolonged starting, blocked rotor, start-on phase reversal and single phasing conditions. Transient

models of induction and synchronous motors have been developed for interfacing with an EMTP program. These models help to simulate three-phase voltage and current wave forms during starting of motors, single-phasing conditions, all types of faults as well as loading and overloading conditions. These abnormalities are simulated to analyze the performance of the proposed integrated motor protection schemes by offline simulation of relaying signals using the PC/AT-based dynamic relay test bench.

Electric arc furnaces are widely used in steel industries, but they cause voltage flicker and introduce harmonics into the system. The proposed hardware is extended for measuring the power quality of transient signal such as flicker severity, unbalances, harmonics, etc. One of the processors compute relative voltage changes using moving average filter, demodulates the signal by squaring demodulator, filters the signal to suppress the noise to retain flicker frequencies, and performs statistical evaluation. The computation of unbalances, harmonics, and other functions are mapped onto other processors. Flicker meter performance is evaluated using transient data obtained from EMTP studies.

The performance of the proposed digital numeric protection has been evaluated using PC/AT-based dynamic relay test bench. The bench performs both steady state and dynamic tests on protective relays. The test procedure simulates realistic three-phase relaying signals and monitors relay operation. The evaluation results have clearly demonstrated the efficacy of the proposed multiprocessor hardware schemes for numeric relaying applications.

References

1. BORNARD, P. AND BASTIDE, J. C. — A prototype of multiprocessor based distance relay, *IEEE Trans.*, 1982, **PAS-88**, 491–498.

2. GAO, Z D. AND WANG, G. B. — A new power swing block in distance protection based on a microcontroller–principle and performance analysis, *IEE Int. Conf. on Advances in Power Systems Control, Operation and Management*, Hongkong, Nov '91, pp. 843–847.

3 ERIKSSON, L. SAHA, M. M. AND ROCKEFELLER, G. D. — An accurate fault locator with compensation for apparent reactance in the fault resistance resulting from remote-end infeed, *IEEE Trans*, 1985, **PAS-104**, 424–436.

4. ZAMORA, J. *et al* — Fault location on two-terminal transmission lines based on voltage, *IEE Proc. C*, 1996, **143**, 1–6.

Thesis Abstract (Ph. D.)

High-voltage trimming of polymer thick film resistors by Y. Srinivasa Rao
Research supervisor: Prof. M. Satyam
Department: Electrical Communication Engineering

1. Introduction

Trimming of resistors is a well-known process in the manufacture of resistors in hybrid circuits using thick-film technology. One of the trimming techniques that has been used is based

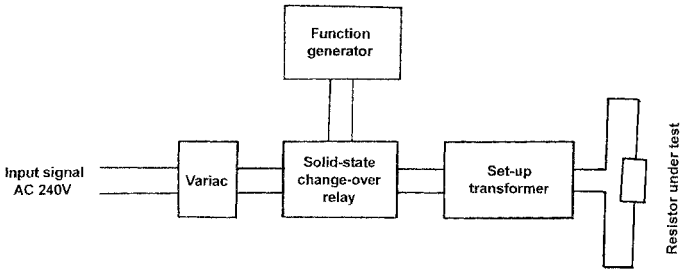

FIG. 1. High-voltage test circuit.

on the application of high-voltage pulses. This technique has been applied, so far, to frit glass-based thick-film resistors. Currently, polymer-based pastes are used to fabricate resistors for economic reasons. These resistors are generally trimmed by laser or abrasive trimming.[1, 2] The possibility of trimming these resistors using high-voltage pulses has been investigated in this work.

2. Experimental work

2.1. *Resistor fabrication*

Polymer paste containing PVC and graphite has been prepared by first dissolving PVC granules in cyclohexanone and then blending graphite into it. This paste has been used for printing resistors on alumina substrates with a screen printer supplied by DeHaart (Massachusetts, USA, model SP-SA-05). These printed resistors are processed using the usual thick film processing of polymer-based films. The heat-treatment involves drying at room temperature for 15 minutes, followed by curing at 100°C for 4 hours. The thickness of the cured samples is found to be in the range of 40 to 150 microns.[1–4]

2.2. *Electrical measurements*

The set-up used to apply high-voltage pulses to the resistors is based on the one described by De Lacy[5] (Fig. 1). It consists of a high-voltage changeover relay, a transformer, a variac, and a function generator. The amplitude of the pulses is controlled through the variac. The pulse duration and the number of pulses are controlled by the function generator and high-voltage changeover relay.

The value of resistance of each of these resistors is measured through voltage–current characteristics for both ac and dc. In the case of pulse measurements, the resistance is measured directly after it is subjected to high-voltage pulses. Typical voltage–current and voltage–resistance (V–R) characteristics are given in Figs 2 and 3. All the measurements were carried out with instruments having an accuracy greater than 1%.

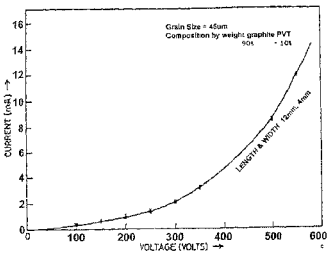

FIG. 2. DC voltage-current characteristics of polymer thick-film resistor.

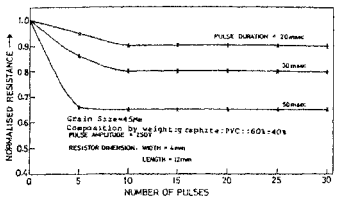

FIG 3 Variation of normalized resistance with number of pulses for different pulse durations.

3. High-voltage effects in polymer thick-film resistors

It has been found that in all the cases mentioned above, resistance decreases if the applied voltage is above a certain threshold value. The change in resistance for different parameters of the voltage and voltage pulses (pulse amplitude, pulse width and number of pulses) has been measured and found that the resistance decreases with increase in amplitude of dc and ac voltages or pulse amplitude, pulse width and the number of pulses. With increase in number of pulses, it is found that resistance decreases initially rather steeply and then stabilizes (slow decrease).

These investigations have been carried out on samples prepared with different compositions of PVC and graphite, in the range of 60% to 90% by weight and with different grain sizes in the range of 10 to 70 microns. In all cases, resistance decreases with the application of high-voltage stimuli.

Experiments have been designed to understand the mechanism responsible for this decrease in resistance (downward trimming) with high-voltage stimuli. It has been concluded that dielectrophoretic forces arising between graphite grains with the application of high voltages are responsible for the downward trimming. Assuming a model for the structure of composite in terms of graphite chains and cavities dispersed in PVC, it has been possible to explain both qualitatively and, to some extent, quantitatively the variation of change in resistance with applied high-voltage stimuli.

The effect of downward trimming on important electrical characteristics of polymer thick-film resistors, namely, current noise and temperature coefficient of resistance have been investigated. It has been found that the current noise decreases after trimming which is attributed to decrease in resistance of resistors after trimming. Variation in the temperature coefficient of resistance also has been explained based on the mechanism responsible for trimming.

4. Conclusions

It may be realised that this high-voltage trimming produces structural changes uniformly throughout the body of the resistor unlike other trimming techniques. Therefore, it is free from problems like current crowding and hot spots. Further, this appears to be highly suitable for trimming embedded resistors as the technique does not call for any heating or bombardment by abrasive. It just involves the application of voltage between the terminals of the resistors. In this technique, it appears that only downward trimming is possible and further investigation is needed to affect upward trimming.

References

1. MURTHY, K. S. R. C., RAMKUMAR, K. AND SATYAM, M. — Electrical properties of PVC–graphite thick film, *J. Mater. Sci. Lett.*, 1984, **3**, 813–816.
2. MURTHY, K. S. R. C AND SATYAM, M. — Curing and thermal cycling process in PVC/graphite thick films, *J. Mater. Sci. Lett.*, 1985, **4**, 1371–1374.
3. MURTHY, K. S. R. C. AND SATYAM, M. — Trimming studies on polymer thick film resistors, *J. Mater. Sci.*, 1987, **22**, 1413–1418.
4. BADRINARAYANA, T., RAMKUMAR, K. AND SATYAM, M. — Mechanism for downward trimming of polymer resistors, *J. Phys. D*, 1992, **25**, 717–721.
5. DE LACY, H. — The assessment of thick film resistors performance by high voltage pulsing, *Proc. Hybrid Microelectronics (ISHM) Symp. Conf.*, 1995, pp. 219–227

Thesis Abstract (Ph. D.)

Studies on the dynamics and control of smart laminated composite beams and plates by Bishakh Bhattacharya
Research supervisors: Profs M. Seetharama Bhat and A. V. Krishna Murthy
Department: Aerospace Engineering

1. Introduction

A broad survey of developments on smart materials and structures[1] has defined three very general characteristics of such structures, (a) with a definitive purpose, (b) with means and imperative to achieve that purpose, and (c) a biological pattern of functioning. In terms of engineering, this requires a structure containing distributed actuators and sensors embedded or surface-bonded with the host structure and a controller to achieve objectives like vibration suppression or shape control. The present work is limited to the first objective of vibration suppression for a class of structures generally known as laminated composite beams and plates. The research in this direction has started almost two decades ago from the seminal work of Crawley and Luis.[2] In this work, a static model of an isotropic beam with embedded/surface-bonded piezoelectric layers is developed. Since then, enormous ramification, in the form of modelling more complex interactions between smart and host layer using different smart materials, has taken place. Research was done on the following aspects by us.

- Development of a new modelling scheme augmenting actuating strain to the structural strain and using variational principle to formulate the equation of motion. This method is applied to develop beam models based on simple Euler–Bernoulli equation to more complex models incorporating the effects of shear deformation, large deformation, rotary inertia and coupling of in- and out-of-plane motions.
- Numerical simulations of the dynamic behaviour of different laminated composite beams with various ply lay-ups, smart lamina location and control grain using a typical smart material (magnetostrictive material). Results corresponding to different modelling schemes are obtained and compared.
- For finite-element analysis of plate structures, a 38-DOF high-precision plate element is developed and for computational efficiency the same element is condensed dynamically to form an 18-DOF element. Numerical simulation of vibration response of plates with different geometric configurations and boundary conditions are carried out and the results are compared with the existing elements. Finally, a smart 38-DOF plate element is developed based on this passive element. The new element is employed to evaluate the dynamic response of laminated plate with different types of patches of smart layer.
- A scheme of placement of sensors and actuators is developed and a realistic design of controller based on output feedback is presented.

2. Modelling and analysis of smart laminated composite beams

In this study, the interaction mechanism between smart and host composite laminate is modelled based on different displacement fields. A typical model of laminated composite beam with smart layers is shown in Fig. 1.

The beam may consist of several composite laminae, and in some of the layers, smart patches of piezoelectric or magnetostrictive materials are placed very closely so that, although discrete, for all practical purposes they may be assumed as a continuous smart layer. The total strain in any layer of the beam consists of two parts; the elastic strain ε_{xs} given by $\varepsilon_{xs} = u' - yv''$ (+ higher order terms, for models which incorporate the effect of shear deformation); ('/' denotes spatial differentiation) and the active strain ε^i_{xa}, present only in the active layer. Thus, the strain in any layer can, generally be written as

$$\varepsilon^i_x = s\sigma^i_{xs} + \delta_{ia}\varepsilon^i_{xa}$$

where, δ_{ia} is the Kronecker's delta and its value is 1 when $i = a$, i.e. for active layer and is zero for other layers.

Models are developed for two types of composite laminate—symmetric and unsymmetric. In the first case, the smart layer effects predominantly the transverse vibration whereas in the second it can control both transverse and longitudinal vibrations. For unsymmetric laminate, starting from a simple Euler–Bernoulli model, more complex models including the effect of shear deformation and rotary inertia are considered. These models are classified as CBT, CBT-C, HOST-1 and HOST-2, respectively. CBT is based on classical beam theory on pure transverse vibration, while CBT-C takes into account the coupling of in- and out-of-plane

FIG. 1.

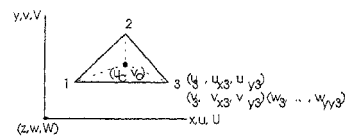

FIG. 2.

vibrations. HOST-1 contains higher order-terms in the assumed in-plane displacement field, whereas HOST-2 includes similar terms only for transverse displacement. HOST-3 is the most generalised model which includes higher-order terms corresponding to both in- and out-of-plane displacement fields.

A comparative study of the vibration parameters like frequency, damping ratio and settling time corresponding to these models is carried out. It is observed, that, in general, the CBT overestimates the frequency and damping of the beam. However, the difference in estimation varies remarkably with the change in span-to-thickness ratio (slenderness ratio) of the laminated beam. Typically, at the slenderness ratio (η) = 25, the frequency estimation of CBT differs from the generalised model HOST-3 by 14.49%, whereas at $\eta = 50$, the difference is only 7.67%. The difference between the frequency estimation of CBT and HOST-3 is more prominent in higher-order modes. Thus, for the same $\eta = 25$, the difference is 22.51% for the second mode and 35.10% for the third mode. A conclusion taken from the numerical simulation is that for slenderness ratio η, below 50, consideration of the higher-order model is essential for accurate estimation of frequency and damping of the beam. Also, it is found that in most of the simulation studies, HOST-3 and HOST-2 give closely matching results. This implies that the consideration of higher-order terms for out-of-plane displacement is more important for the present cases.

Albeit analytical solutions are very useful for getting insight of the system behaviour, unfortunately closed-form solutions are not obtainable in many cases due to structural and geometric complexities. A smart 6 DOF beam element is developed to enable consideration of various boundary conditions and complex geometries. The stiffness, mass and damping matrices corresponding to this element are obtained in closed form, which has made it computationally efficient. The performance of the finite-element analysis is compared to that of the analytical results for a simply supported composite laminate. It is found that the differences in damped frequency estimations between FEM and analytical method are 0.034% for the first mode, 0.46% for the second, 2.04% for the third and 11.91% for the fourth mode of vibration. The finite-element model has subdivided the beam into 12 elements for this analysis. It is observed that further mesh refinement reduces the difference between the higher frequencies obtained by finite-element analysis and analytical solution.

3. Modelling and analysis of laminated composite plates

This study is carried out in three phases. In the first phase, a 38 DOF high-precision finite element is developed. The transverse displacement is represented by a quintic polynomial series

and the inplane displacement by a cubic polynomial series. The element configuration is given in Fig. 2.

In each element, three field displacements u, v (inplane displacements) and w (transverse displacement) are considered along x, y and z directions, respectively. Nodal DOF chosen are grouped into three vectors as,

$$\{\delta\} = \{\{U\}^T, \{V\}^T, \{W\}^T\}$$

where

$$\{U\}^T = \{u_1, u_{x1}, u_{y1}, u_2, \ldots, u_{y3}, u_c\}_{10\times 1}$$

$$\{V\}^T = \{v_1, v_{x1}, v_{y1}, v_2, \ldots, v_{y3}, v_c\}_{10\times 1}$$

$$\{W\}^T = \{w_1, w_{x1}, w_{y1}, w_{xx1}, w_{xy1}, w_{yy1}, w_2, \ldots, w_{yy3}\}_{18\times 1}$$

To make this element more computationally attractive, in the second phase, the element DOF is reduced through dynamic condensation and a new 18-DOF element is formed. Finally, in the third phase, a new 38-DOF high-precision smart element is formed. In this element, the effect of discretely distributed actuators and sensors is incorporated.

Numerical simulations are carried out for laminated plates with various geometric and boundary conditions, using finite elements. The performance of present elements is compared to existing elements on the basis of frequency estimation. In case of a cantilever swept composite plate, for example, the non-dimensional frequency parameter corresponding to a ply sequence $[15_2/0]_s$ is 1.99 in Lee's method and 1.90 in the present method. Although the active DOF are 216 in the present method and 224 in Lee's method, the computational time is found to be three times faster in the present method due to the use of closed-form expression.

A smart plate element is used for finding vibration response of laminated plates with various complex boundary conditions. In a typical example, a clamped circular plate with a patching of smart layer is chosen for simulation. It is found that settling time for vibration suppression changes drastically when the coverage is increased from 0 to 25%, moderately from 25 to 50% and very little onwards. The simulation indicates that a good scope of patch optimization is possible using the present element for such typical cases.

4. Placement of actuators/sensors and design of controller

In the last course of study, two relatively new issues of smart structural control are addressed. These are: (a) placement of smart actuators and sensors on laminated composite beams, and (b) design of a realistic controller for smart structural system. Constant gain velocity feedback controller, chosen in earlier studies, was for the advantage of gaining unconditional stability. However, in this phase of research, a more realistic output feedback controller is chosen. The placement of sensors and actuator patches is carried out on the basis of evaluating the controllability and observability grammian. The intersection space of these two grammians is found out and a modal projection of the intersection subspace is used for the goodness measure of the particular location.

In a numerical study, a smart laminated composite canitilever beam (whose FEM model is already developed in the first phase of research) is considered. The beam consists of 12 ele-

ments. For controlling the first four modes of this beam, three actuator patches and six sensor patches are to be chosen out of 12 available patch positions. The elements are numbered as 1...12 starting from the fixed end. All the possible combinations of actuator and sensor patches are studied and the goodness measure corresponding to the first four modes are obtained. It is found that the actuator set 1, 2, 4 and the sensor set 1, 2, 4, 7, 8, 10 are the best placement positions. A low-order output feedback control algorithm developed by Asthana[3] is applied for the same beam. The controller is found to achieve damping corresponding to the first three modes as 24.47%, 17.49% and 21.53%, respectively, which shows rich potential of designing practical controllers based on this principle.

4. Conclusions

The usefulness of the basic approach of augmenting actuation energy with the strain and kinetic energy of the structure is stressed. Various beam and plate vibration models based on this principle are successfully simulated and interesting insights into the zone of applicability of each model are obtained. The method of actuator and sensor placement and controller design may also guide to the design of efficient and practically implementable controllers for smart structures.

References

1. SPILLMAN, W. B., SIRKIS, J. AND GARDINER, P. T. — *Smart structures and material: What are they? Survey results, J. Smart Mater Struct.*, 1996, **9**, 121–150.
2. CRAWLEY, E. F. AND LUIS, J D. — *Use of piezoelectric actuators as elements of intelligent structures, AIAA J.*, 1987, **25**, 1373–1385.
3 ASTHANA, C. B. — *Low-order output feedback controller design with application to missile autopilots*, Ph. D. Thesis, Indian Institute of Science, Bangalore, 1998.

Thesis Abstract (Ph. D.)

Turbulent free convection over horizontal surfaces by S. Ananda Theerthan
Research supervisor: Prof. J. H. Arakeri
Department: Mechanical Engineering

1. Introduction

This work deals with turbulent-free convection in a horizontal fluid layer above a heated surface. This type of convective flow is encountered in many industrial and natural situations. Examples include solar collector, the solidification process in metal casting, crystal growth, earth's mantle convection and convection in the earth's atmosphere, and evaporative cooling driven by natural convection.

Free convection over a horizontal surface or between two horizontal surfaces, kept one above the other, is more complicated than flow adjacent to a heated vertical surface where

there is a preferred direction of motion. In contrast, still fluid above a heated horizontal surface will transmit heat solely by conduction until buoyancy forces overcome the diffusion of heat and viscous effects. When motion is set up, warm fluid ascends through the denser surrounding fluid while the denser fluid descends simultaneously. This type of motion has in it more complicated flow structures like plumes and thermals, apart from boundary layers. Turbulent-free convection of this type, especially Rayleigh–Bénard convection, has been studied extensively. See Sigga[1] for a recent review.

The present work contains two main parts. One is the development of a new model for near-wall dynamics of turbulent convection over heated surface. The second is an experimental study of the heat-transfer coefficient and near-wall flow structure under different conditions. From earlier studies, it is clear that no satisfactory model has been proposed for the near-wall flow structure in turbulent convection over a heated surface at moderate *Ra*. Howard's theory[2] is for intermittent eruption of thermals which, however, is not often observed in experiments. Various power laws, based on mixing length arguments, have been proposed for variation with distance in the vicinity of the wall of mean temperature and temperature fluctuations.[3, 4] These theories, however, haven't found experimental verification (see for example Somerscales and Gazda[5]). We propose a model for the near-wall structure using which we obtain results for plume spacing, distribution of mean temperature, rms fluctuations of temperature and of horizontal and vertical components of velocity. The regions we are considering are the conduction layer and the plume region (what is called by Castaing *et al.*[6] as the mixing zone). The basic idea is that we model the turbulent flow near the wall as an array of 'coherent structures'. The coherent structure we recognize from experiments is the line plume.

The second part of the work involves the study of planform structure of convection and heat-transfer rates under different conditions. These conditions correspond to Rayleigh–Bénard convection (RB) (bottom plate heated and top plate cooled), unsteady non-penetrative convection (UNP) (bottom plate heated and top plate insulated) and unsteady, open convection (OC), where top fluid surface is open to ambient. Also, another experiment was performed to study the effect of large-scale flow on heat transport and flow structure. In this experiment, an external circulation is imposed on a heated surface (LF). The basic idea is to have the external circulation simulate large-scale flow in Rayleigh–Bénard convection at high *Ra*. The length scales are obtained through videographs and image analysis and compared with model predictions. A new method of normalizing heat-transfer rate is proposed so that a comparison can be made of the heat-transfer rates under different conditions.

2. Results and discussion

2.1. *A model for the near-wall dynamics*

The model for the near-wall dynamics based on experimental evidence consists of laminar boundary layer and an array of steady, 2D line plumes. The model reproduces the distributions of mean temperature, rms temperature fluctuations and rms vertical velocity fluctuations close to the wall, reasonably well. The deviations observed in the case of rms horizontal velocity fluctuation is due to large-scale flow present in the experiments which is not accounted for in

the present model. The model predicts that the Rayleigh number based on plume spacing (λ_c), $Ra_{\lambda_c}^{1/3} = 52\,\mathrm{Pr}^{-0.012}$; the dependence on Prandtl number is thus weak.

2.2. *Experimental results*

We summarize the following mean results from the experiments conducted with different configurations.

- The experiments confirmed that randomly moving line plumes are the dominant mechanism of heat transport close to the wall.
- The LF (convection with an external flow) experiments, done to mimic high Ra RB, clearly established that an imposed flow aligns the plumes in flow direction. Further, the flow reduces heat-transfer rate for a given temperature difference.
- Three types of planform structure were identified in the OC experiments, viz. cells, broken lines and aligned lines. At low fluxes, the cells resemble the type of planform we obtain in RB convection. At high fluxes we start getting broken lines and especially at low AR, we get aligned plumes, presumably, due to a large-scale velocity generated inside the convection cell by top-evaporating free surface. These aligned line plumes resemble the type of planform we obtain when an external flow is imposed on LF. The sideviews for OC at high fluxes show inclined dye lines when AR is low suggesting again a large-scale flow is present.
- For the OC experiments the average plume spacing (λ) nondimensionalized using the heat flux $Ra_{\lambda_f}^{1/4}$ varies between 25 and 50 and that nondimensionalized using the temperature difference $Ra_{\lambda}^{1/3}$ varies between 40 and 90. At higher fluxes the plume spacings are close to model predictions.
- In the UNP experiments, $Ra_{\delta_T}^{-1/3}$ (representing the nondimensional heat-transfer rate) is nearly constant with change in AR and Ra and $\simeq 0.13$. This value of $Ra_{\delta_T}^{-1/3}$ is obtained at $Ra \simeq 10^{11}$ in RB. In the OC experiments, $Ra_{\delta_T}^{-1/3}$ lies between 0.1 and 0.2, and shows dependence on Ra_*, and AR. In the OC experiments, the ratio of top heat flux to bottom heat flux depends on aspect ratio and the effect of these two parameters cannot be dellineated.
- In the above experiments, we observe for a given heat flux, an increase in the value of ΔT with decreasing aspect ratio, similar to an increase in the value of ΔT obtained when an external flow is imposed.

3. Conclusions

A model has been proposed for the near-wall dynamics of turbulent-free convection over horizontal surfaces. The model agrees reasonably well with the experimental results in the litera-

ture. Experimental results show three types of planform structure on a heated horizontal surface. The-heat transfer results indicate the influence of large-scale flow as heat-transfer rate reduces for the same temperature difference when large-scale flow is present.

References

1. SIGGIA, E. D. — High Rayleigh number convection, *A Rev. Fluid Mech.*, 1994, **26**, 137–168.
2. HOWARD, L. N. — Convection at high Rayleigh number, *Proc. 11th Int. Cong. Appl. Mech* (H. Gortler, ed.), Springer, 1966, p. 1109.
3. KRAICHNAN, R. J. — Mixing-length analysis of turbulent thermal convection at arbitrary Prandtl number, *Phys. Fluids*, 1962, **5**, 1374–1389.
4. MALKUS, W. V. R. — The heat transfer and spectrum of thermal turbulence, *Proc. R Soc. Lond. A*, 1954, **225**, 195–212.
5. SOMERSCALES, E. F. C. AND GAZDA, I. W. — Thermal convection in high Prandtl number liquids at high Rayleigh numbers, *Int. J. Heat Mass Transfer*, 1969, **12**, 1491–1511.
6. CASTAING, B. *et al.* — Scaling of hard turbulence in Rayleigh–Bénard convection, *J. Fluid Mech.*, 1989, **204**, 1–30.

Thesis Abstract (Ph. D.)

Evolution and instability of unsteady boundary layers with reverse flow by Debopam Das
Research supervisor: Profs J. H. Arakeri and V. H. Arakeri
Department: Mechanical Engineering

1. Introduction

This work deals with the evolution and instability of wall-bounded unsteady velocity profiles with reverse flow. Such flows occur, for example, during unsteady boundary-layer separation and in oscillating pipe flow. The work is divided into two main parts. Part I deals with unidirectional flows—the main focus is on the instability of the inflectional velocity profiles which are changing with time. A new analytical solution is obtained for unsteady unidirectional flow when the time-dependent volume flow rate is prescribed. In part II, the evolution of the inflectional velocity profiles are investigated when the profiles change both in space and time.

We have developed a novel experimental technique to study unsteady velocity profiles with reverse flow. The principle of these experiments is illustrated below. We generated motion in a long pipe with a piston. The piston accelerates from zero velocity to U_p for time, $0 < t < t_0$, maintains constant velocity for $t_0 < t < t_1$, decelerates to zero velocity for $t_1 < t < t_2$, and is stationary for $t > t_2$. These velocity profiles are unsteady and have inflection point, hence become unstable at relatively low Reynolds numbers. The instability and evolution of such flows is the main focus of this study. These experimental results are simpler to analyse because there is no streamwise variation of the pressure gradient and no residual effects from previous cycles. This

helps in understanding the mechanism of initial development of the flow through the analysis of linear stability characteristics of the velocity profiles.

In the second part, we study experimentally the evolution of unsteady flow when both temporal and spatial variation of the pressure gradient is present. To include the axial variation of the pressure gradient the cross section in the channel is varied with distance by modifying one wall of the channel. We have studied the flow past a curved surface in a channel with four different geometries: three diffusers having different lengths and curvatures, and a 2D rectangular step.

2. Experimental

The experimental arrangement is a closed loop, clamped to a wooden board. Glass pipes of 2.56-cm diameter and 145-cm long form two legs of the loop. They are connected with PVC pipes at either end. Pipe 1 contains a piston while pipe 2 contains the test section. One end of the piston is connected through an inextensible string to a stepper motor; the other end is simultaneously connected to a ten-turn 1 kΩ potentiometer. The pulley fixed to the potentiometer shaft has 3-cm diameter and has a spiral groove cut on the surface on which the string sits. The output signal from the potentiometer is stored in an oscilloscope and is subsequently used to get piston velocity as a function of time. The light from a light-emitting diode, connected with the stepper-motor controller and kept below the test section, is recorded by a video camera simultaneously with the flow structure. This signal gives the time of starting of the motor and the time when the motor is switched off. In all cases, the distance of the piston travel was such that disturbances from the bends did not convect to the test section during the time of the experiment. Dye and particle visualization techniques have been used in the present study. Hot wire measurements obtained using a constant temperature anemometer (Dantec 56C01 CTA with 56C17 CTA bridge) were mainly used to get the transition-to-turbulence times. A few experiments have been carried out in a channel with rectangular cross section. The principle of these experiments are same as that in the pipe.

In part II, one wall of the channel was modified to obtain the streamwise variation of the pressure gradient (i.e. pressure gradient is both function of streamwise distance, x and time, t). As in part I experiments, the piston motion consists of acceleration, constant velocity and deceleration to rest phases.

The two parameters that can be varied in our experiment are the Reynolds number and boundary-layer thickness, δ_1. Reynolds number ($Re_{\delta 1}$) based on δ_1 and the centerline velocity at t_1 (u_{max1}) ranges from 250 to 3,000 and the range of δ_1/R and δ_1/H is between 0.1 and 0.91.

3. Results and discussion

In the pipe, we observe from flow visualization that the flow becomes unstable with the formation of what appears to be a helical vortex. In channel, we have observed two-dimensional Kelvin–Helmholtz-type vortices. From our flow visualization studies we note the following main observations:

i) Instability of the inflectional point profiles, as in the case of Kelvin–Helmholtz instability, results in the formation of a series of vortices. In the cases we have studied, the critical $Re_{\delta i}$ below which the flow does not become unstable is about 500.

ii) Nearly periodic arrays of vortices appear in both top and bottom half of the pipe (and channel) as the instability develops.

iii) For $Re_{\delta i}$ smaller than a critical value, ($\simeq$ 1200) the vortices do not breakdown to turbulence. When they do breakdown the transition is very rapid.

iv) When vortices are formed away from the wall they grow with time and move towards the centre of the pipe. There is strong interaction between the vortices which results in distortion and the final breakdown to turbulence.

v) Secondary vortices are observed at higher $Re_{\delta i}$. Sometimes, primary and secondary vortices form a pair take the shape of a mushroom and move rapidly towards the centre. In some cases, the vortices turn in the direction of the flow at the centre and form a single vortex before breakdown.

vi) Coalescence between the two primary vortices at the same wall and sometime between vortices of the opposite wall has been observed.

We have experimentally observed instability results in vortex formation and its breakdown makes the flow turbulent. Keeping in mind that our aim is to understand the evolution of the reverse-flow-type velocity profiles, we measure the times when the wave appears, when vortex forms, and when transition occurs and the wavelength when the wave appears. The wavelength of the instability $\simeq 3\bar{\delta}$, where $\bar{\delta}$ is the average boundary-layer thickness, the average being taken over time the flow is unstable. The time of formation of the vortices scales with the average convection time scale and is $\simeq 33/(\overline{(\Delta u/\delta)})$, where $\Delta u = (u_{\max} - u_{\min})$ and $u_{\max}$, $u_{\min}$ and δ are the maximum velocity, minimum velocity and boundary-layer thickness, respectively, at each instant of time. The time to transition to turbulence is $\simeq 39/(\overline{(\Delta u/\delta)})$. Quasi-steady linear stability analysis of the velocity profiles bring out two important results. First, the stability characteristics of velocity profiles with reverse flow near the wall collapse when scaled with the above variables. Second, the wave number corresponding to maximum growth does not change much during instability even though the velocity profile does change substantially. Using the results from the experiments and the stability analysis, we are able to explain many aspects of transition in oscillating pipe flow.

We conducted some preliminary experiments to understand the initiation of unsteady boundary-layer separations. As in the straight pipe and channel experiments, the unsteady piston motion provided temporal change in pressure gradient, but, in addition, the spatial change was introduced by having a cross-sectional area change. The classical unsteady separation process was observed in the case of flow in the rapidly changing cross section—elliptically indented channel. A reverse flow region appears near the leading edge which grows into a single vortex. The subsequent evolution of the flow, i.e. the formation of secondary vortices, etc.

and their interaction(s), depends on the Reynolds number, geometry and piston deceleration history. A number of different interactions have been observed in our experiments.

It appears that the instability of the inflectional point profiles with reverse flow results in the formation of the vortex. In the few cases we have studied the time of formation of the vortices is $\sim 35/(\overline{\Delta u}/\overline{\delta})$. More experiments are needed to confirm this relation.

4. Conclusions

The simple trapezoidal piston motion allows us to study the instability and transition of unsteady inflectional point profiles. The time of vortex formation is approximately $33\,\overline{\delta}/\overline{\Delta u}$, the transition time is $\sim 39\ \overline{\delta}/\overline{\Delta u}$ and the wavelength of the instability is $\sim 3\ \overline{\delta}$. At low Reynolds numbers ($Re_{\delta 1} < 500$) instability is not observed and transition to turbulence is observed only for $Re_{\delta 1} \geq 1200$.

References

1. AKHAVAN, R., KAMM, R. D. AND SHAPIRO, A. H. — *J. Fluid Mech.*, 1991, **225**, 395–422.
2. AKHAVAN, R., KAMM, R. D. AND SHAPIRO, A. H. — *J. Fluid Mech.*, 1991, **225**, 423–444.
3. GAD-EL-HAK, M., DAVIS, S. H., MCMURRAY, J. T. AND ORSZAG, S. A. — *J. Fluid Mech.*, 1984, **138**, 297–323.
4. MCALISTER, K. W. AND CARR, L. W. — *Trans. ASME J. Fluids Engng*, 1979, **101**, 376–380.
5. WEINBAUM, S. AND PARKER, K. — *J. Fluid Mech.*, 1975, **69**, 729–752.

Thesis Abstract (Ph. D.)

Extrusion processing of aluminium–lithium alloy 1441 by G. Chandramohan
Research supervisor: Prof. E. S. Dwarakadasa
Department: Metallurgy

1. Introduction

The efficiency and performance of aircraft structures would greatly benefit from the use of lighter materials. The addition of lithium to aluminium gives the greatest reduction in density and increase in elastic modulus of any alloying elements and Al–Li–X system has recently been the subject of intensive studies. Alloys developed for commercial exploitation include AA 8090 and 2090. In these alloys, a 10% lower density with 10% higher elastic modulus seems to be possible which can bring about a 30% weight reduction in aircraft. But the ductility and fracture toughness of these alloys is low. In the recent past, Al–Li alloy 1441 having better ductility and fracture toughness has been developed at the expense of some strength by

the former Soviet Union. The properties of these alloys are known to much lesser extent. This alloy has therefore been chosen for the present study.

The current industry assessment is that for a large modern transport aircraft the extrusion product form may be as high as 28 wt% of the total product form. Thus, a study in detail on the extrusion processing of this alloy is necessary.

The objectives of the present investigation are to find out the optimum processing conditions for extruding Al–Li alloy 1441 and to study the effects of extrusion processing variables such as extrusion temperature, ram speed, reduction ratio and die design on the mechanical properties of extruded/extruded and heat-treated Al–Li alloy 1441.

2. Materials and methods

2.1. *Processing*

The alloy was prepared using a well-established ingot metallurgy technique.[1] Cast ingots were homogenized at 530°C for 30 h. They were then scalped to 75-mm diameter and 200-mm length for extrusion processing. Extrusions were carried out at various combinations of processing parameters using a 5-MN hydraulic press available at the National Physical Laboratory, New Delhi. Extrudates were heat-treated to various aging conditions.

2.2. *Experimental techniques*

Mechanical tests were carried out using a servo hydraulic testing machine. An Olympus microscope was used for microstructural examination of extrudates. Fracture surfaces were examined using a scanning electron microscope. TEM studies were carried out to determine the subgrain size and precipitates present at the grain boundary and in the matrix.

3. Results and discussion

3.1. *Hot-compression testing*

In order to understand the behaviour in extrusion, hot deformation characteristics of alloy 1441 were studied. Hot-compression tests were carried out on homogenized samples at several temperatures and strain rates to plot deformation mechanism maps from which safe zones for processing were determined and constitutive equations established.

The specimen deformed at 350°C and 10 s^{-1} shows instability in the form of grain boundary cracks whereas a specimen deformed at 500°C and 0.01 s^{-1} shows fully recrystallized structure. The presence of T_2 phase at the grain boundaries may be the cause for grain-boundary cracks when deformation is carried out at 350°C. It is reported[2] that when annealing carried out at 350°C, T_2 phase is formed in Al–Li alloys having Cu : Mg ratio of 1.7. A more suitable constitutive equation for a wide range of strain rates is given as $\dot{\varepsilon}\ \exp(Q/RT) = [\sinh(\alpha\sigma)]^n$. The hot-working constants A, α, n, Q, were determined using the minimization technique developed by Sheppard and Wright.[3] Stress exponent of 4.1 and activation energy of 149 kJ/mole implies the mechanism of deformation to be dislocation climb. The constitutive

equation developed for this alloy is $\dot{\varepsilon}\ \exp(149000/RT) = e^{24.3}\ [\sinh(0.025*\sigma)]^{4.1}$ and is usable in modeling of hot deformation processes.

3.2. *Properties of extrudates*

In general, extrusions produced microstructures which varied over the cross section; the layer immediately adjacent to the surface was fully recrystallized and the mid-radius location was partially recrystallized while the core structure remained essentially unrecrystallized. Recrystallization increased with increasing temperature, extrusion ratio and ram speed. The variation in microstructure from the centre to surface is due to different strains and temperatures existing over the cross section during extrusion. The surface of the material experienced high strain during deformation resulting in recrystallized structure. Temperature of the surface is also higher due to high frictional forces encountered. The combined effect of higher strain and lower temperature on the subgrain morphology was also noted.

It is observed that higher initial billet temperature results in higher UTS and 0.2% PS. It is observed that the properties are the highest for extrusion ratio of 36:1 when extruded at 500°C. Extrudates produced at lower temperatures might have contained previously documented Al–Cu–Li–Mg-based T_2 particles.[4, 5] In the present study also, the minimum proof stress and UTS were obtained for extrusions carried out at a temperature of 350°C and extrusion ratio of 16:1 where solutionising would not have taken place. Increase in UTS and PS with increasing temperature and extrusion ratio is due to solutionising effect, since increased thermal energy or conversion of work into heat during the process (for higher extrusion ratios) produces greater solutionising effect.

It is reported that streamlined dies facilitate the use of small extrusion ratios in producing uniform microstructures across the cross section without causing defects commonly associated with shear dies.[6] However, in the present study, it was found that microstructures at centre and surface were different when streamlined die was used. The frictional forces were higher due to larger contact area at the billet–die interface when streamlined die was used. As the temperature difference increases from surface to core, microstructure also changes from surface to core. Incipient melting was also observed on the surfaces of extrudates produced using streamlined die due to large amount of frictional heat evolved. Extrusion pressure required for streamlined die was 1.8 times that of shear die.

It is seen from SEM fractographs that planar slip and grain-boundary cracks were the main features of fractured surfaces. The fracture surface of extrudate processed at low temperature and low extrusion ratio has more dimples, as δ' precipitates were not present in the extrudates. Planar slip and grain-boundary failure were seen for extrusion carried out at high extrusion ratio and high temperature.

Tensile properties of 1441 are compared with 8090 alloy processed under the same extrusion conditions (Table I).

As Li is less and Cu is more, more S' and less δ' are formed in 1441 alloy. As large number of S' precipitates disperse the slip,[7] planar slip is reduced in 1441 alloy which is reflected in fractographs and elongation values.

Table I
Tensile properties of 8090 and 1441 alloys

Alloy	UTS (Mpa)	0.2% PS (Mpa)	% elongation	Stress-intensity factor (Mpa $m^{0.5}$)
8090	440	372	5 1	9 2
1441	419	343	11.0	15.9

3.3. *Properties of heat-treated extrudates*

The influence of extrusion process parameters on extrudates after heat treatment was studied to select the optimum extrusion process parameters for heat-treated extrudates. Optical microscopy revealed that some degree of grain growth had occurred during the solutionising treatment at the surface, but the core remained unrecrystallized. In the peak aged condition, well-developed δ′ particles and bull's eye structure (δ′ on Al_3Zr particles) were observed. Homogeneous distribution of S' and T_1 precipitates was also observed in TEM micrographs. The precipitation of S' was uniform due to higher (Cu + Mg) content in this alloy.

The tensile tests revealed that mechanical properties are influenced by extrusion process parameters and precipitation reactions. Increase of tensile properties due to aging was higher for low-temperature extrudates compared to high-temperature extrudates due to natural aging effects for the extrudates produced at high initial billet temperature. The ductility of this material decreased with respect to aging time. With aging, the number density or coarse copper-rich T_2 precipitates and PFZ (precipitate-free zone) adjacent to the grain boundaries.

All aged materials have shown the same overall fracture behavior which is one of increasing intergranular boundary failure with increasing aging time. Dimples were observed in the under-aged samples since precipitation had just started in these samples. Intergranular boundary failure observed in the over-aged sample was due to the presence of δ′ and soft PFZ at the grain boundaries.

It was observed that SRS (strain-rate sensitivity) was negative for solutionised, under- and peak-aged samples and it was positive only for the over-aged samples. Compression tests were conducted on aged samples at temperatures of 180, 200, 220 and 300°C. It was found that flow stress decreased with increase in strain rate up to a temperature of 200°C, but at 220°C, flow stress increased with increase in strain rate. SRS was positive above 220°C since dissolution of δ′ precipitates takes place at 220°C.[8] These results indicated that δ′ is primarily responsible for serrations in Al–Li alloy 1441.

4. Conclusions

The best properties are obtained for extrusions carried out at a temperature of 500°C and an extrusion ratio of 36:1 where both the solutionising effect and the recrystallization effect seem to be optimized.

Streamlined die design was not effective in decreasing the extrusion pressure. In fact, it was not possible to extrude the alloy at all.

Precipitation events influence the mechanical properties of heat-treated extrudates.

1441 alloy has better ductility and fracture toughness compared to 8090 alloy.

The occurrence of serrations in the stress–strain curve is due to the presence of fine $\delta'(Al_3Li)$ precipitates.

Results have been used to suggest the most optimum extrusion working parameters for the Al–Li alloy 1441.

References

1	DWARAKADASA, E. S., SASTRY, D. H. AND PRASAD, Y. V. R. K.	*Closure report of AR & DB project on high strength aluminium alloys*, Grant No. Aero/Rd-134/100/10/82-83/357.
2.	BALL, M D AND LAGACE, H.	In *Aluminium–lithium alloys III* (C. Baker, *et al.* eds), The Institute of Metals, London, 1986, p. 555.
3.	SHEPPARD, T. AND WRIGHT, D. S.	*Metals Technol.*, 1979, p. 215
4.	MUKHOPADHYAY, A. K., FLOWER, H. M. AND SHEPPARD, T.	*J. Phys.*, 1987, **48**, C3–219.
5	MUKHOPADHYAY, A. K., ZHOU, D. S. AND YANG, Q. B.	*Scr Met. Mater.*, 1992, **26**, 237.
6.	PRASAD, Y. V. R. K.	*Indian J. Technol*, 1990, **28**, 435.
7.	GREGSON, P. J. AND FLOWER, H. M	*Acta Metall.*, 1985, **33**, 527.
8.	SATYAPRASAD, K. *et al.*	*Scr. Metall*, 1994, **30**, 1299.

Thesis Abstract (Ph. D.)

Development of liquid-phase co-spray forming and its application to Al–SI–PB alloys by Yu Fuxiao
Research supervisors: Profs E. S. Dwarakadasa and S. Ranganathan
Department: Metallurgy

1. Introduction

Spray forming is a process that combines atomisation and deposition. During the atomisation stage, a stream of molten metal is disintegrated into a fine dispersion of droplets using high-energy inert gas. The resultant distribution of droplets of various sizes and thermal histories is directed by the atomising gas towards a substrate, where it impacts and builds up into a deposit of predetermined shape. The distinct features of the spray-formed products are the fine equi-axed structure and low segregation level. Extended solid solubility of alloy elements in some alloys may take place.[1, 2]

The objective of the present work is the development and understanding of a new technique, namely, liquid-phase co-spray forming (LPCSF). The selection of Al–Si–Pb alloys for

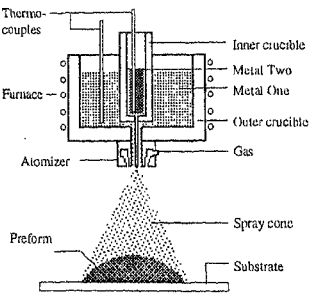

FIG. 1 Schematic of liquid-phase co-spray forming (LPCSF).

this study was based not only on the fact that Al–Si–Pb alloys are potentially good plain-bearing materials but also because they are difficult to produce by other solidification processes.

It was found necessary to investigate the microstructural evolution during spray forming because LPCSF was developed based on the principles of spray forming. This consideration came from the fact that the solidification nature (rapid or slow) of spray forming and the mechanisms governing the microstructural evolution are still a matter of debate.[1] For this purpose, a near-eutectic Al–Si alloy (LM6) was spray formed under various conditions.

LPCSF process was used to fabricate Al–Si–Pb alloys with nominal compositions of Al11.5Si–15Pb and Al8Si–10Pb, respectively, at relatively low pouring temperatures. The alloys thus formed were then given a secondary processing (hot extrusion) to minimise porosity and investigate the microstructure evolution during hot extrusion. Following hot extrusion, room-temperature tensile tests were conducted on the extruded rods.

2. Liquid-phase co-spray forming

Figure 1 shows the schematic representation of liquid-phase co-spray forming. It differs from spray forming in the use of two crucibles that separate the liquid phases before atomisation. The temperatures of the two liquid metals may be maintained individually or kept the same before atomisation according to the specific system or other considerations. Upon pouring, the two liquid phases flow down through the metal delivery tubes and meet at the tip of the atomiser exit. The composition of the preform to be produced depends on the deposit rate ratio of the different liquid phases which in turn depends on the ratio of the flow rates of the two liquids at the atomiser exit. The term liquid-phase co-spray forming is given to this technique to emphasise the difference between the LPCSF process and atomisation and co-deposition process that is generally employed to produce metal matrix composites (MMCs).

Table I
Experimental conditions in spray forming

Expl nos	Gas	Pressure (MPa)	Metal flow rate (g/s)	Substrate	Distance (cm)	Melt temp. (K)	Others
1	N_2	1.2	30	Steel	22	1003	
2	N_2	1.2	35	Copper	32	1003	
3	N_2	1.2	35	Copper	32	1003	*

*melt was prepoured before atomization

3. Experimental work

3.1. *Spray forming and liquid-phase co-spray forming*

The atomizer employed in this work is of an annular confined type. A resistance furnace is on the top of spray forming chamber where spray forming is performed. During the melting of the alloy, the temperature of the alloy in the crucible is continuously monitored by an alumel–chromel thermocouple. A stationary substrate is placed below the atomizer at a fixed distance. The pressure of the inert gas used for atomization is controlled by a gas regulator.

By spray forming LM6 alloy (wt%, Si, 11.47, Fe, 0.37, Cu, 0.19, Mg, 0.18, Al bal.), three experiments were conducted in the ambient air under different conditions. Three bell-shaped preforms with heights of about 40 mm from bottom to top were obtained (Table I). The over-sprayed powders produced in each experiment were collected for the microstructure and surface morphology studies.

By liquid-phase co-spray forming Al11.5Si–15Pb and A18Si–10Pb, two experiments were performed in the open air. Two bell-shaped preforms of height of about 60 mm along the central axis were obtained. The Al–Si alloys used in two experiments are LM6 and a diluted LM6 alloy (wt%, Si, 8.05, Fe, 0.24, Cu, 0.18, Mg, 0.14, Al bal.), respectively. Commercial-purity Pb was used. In each experiment, the Al–Si alloy and Pb were charged in the outer and inner crucible (Fig. 1 and Table II, respectively). The over sprayed powders were collected for microstructure and surface morphology studies.

3.2. *Extrusion and room-temperature tensile test*

Two cylindrical billets of size of 45-mm diameter × 50-mm length machined from the LPCF formed preforms were hot extruded in a CBJ-250-ton hydraulic press with a die container diameter of 50 mm at 573 K. The billet obtained from the first experiment was extruded into a 60-mm-diameter cylindrical rod under an extrusion ratio of 9.8. The billet obtained from the second experiment was extruded into a rod of diameter 12 mm corresponding to an extrusion ratio of 17.4.

Tensile specimens corresponding to ASTM (E-8) standard were machined from the extruded rods. The tests were conducted at room temperature using a Servo hydraulic test machine (Instron model 8502) at an initial strain rate of 5×10^{-4}. From the engineering stress–strain curves recorded, 0.2% proof yield stress, ultimate tensile stress (UTS) and elongation (%) to fracture were measured. Based on the true stress–strain curves, plotted corresponding

Table II
Experimental conditions in LPCS

Expt no	Gas	Pressure (MPa)	Sum of metal flow rates (g/s)	Substrate	Distance (cm)	Melt temp (K)
1	N_2	1.6	75	Copper	50	1003
2	N_2	1.6	75	Copper	50	1123

to engineering stress–strain curves, work-hardening rates were calculated via true strain and plotted.

3.3. *Microstructural characterisation*

Microstructures of preforms of oversprayed powders were studied both by optical and scanning electronic microscopy (SEM) following standard metallographic procedures in different locations and under different conditions.

4. Result and discussion

A microstructure consisting of equiaxed Al grains with equiaxed Si particles located on the grain boundaries was observed in the central regions of all the spray-formed preforms (Fig. 2). This microstructure differs from that of oversprayed powders where only fine cells and/or dendrites of primary Al plus interdendritic eutectic are shown. This microstructure also shows no similarity to the microstructure of the Al–Si alloys generated by any other solidification method.[3–5] This indicates that the mechanisms governing the formation of equiaxed microstructure during spray forming are unique. Thus, solidification during deposition starts from a semi-solid state leads to the question of the essential difference between deposition and other semi-solid processes such as liquid-phase sintering and stircasting. This difference is brought out by the fact that during deposition the impact of full liquid droplets results in a relative solute–poor liquid film surrounding the solidified dendirtic blocks, while during other semi-solid processing the liquid is more or less in equilibrium with solid. The net effects of this solute–poor liquid film are retardation of grain boundary migration and reduction of overall solute segregation. It is clear that during deposition the cooling rate experienced by the deposit was low; otherwise, the microstructure should show the microstructure produced by atomisation as well as the rapidly solidified microstructure of the liquid films.

Comparison of the microstructures in the bottom regions of preforms spray formed in the second and their experiments revealed that the substrate-dominant cooling as defined by Suresh and Doherty[6] may not be a sufficient condition leading to the fine structure usually observed in the spray formed preforms.

The microstructures in the LPCSF-formed preforms are, if the presence of Pb particles is not taken into account, similar to that in the spray-formed preforms, in spite of Si concentration. This means that LPCSF and spray forming share the same principles. In the equiaxed region of the preforms, most of the Pb particles were found distributed uniformly on the Al grain boundaries along Si particles, while lesser quantity of Pb particles locate in the interiors of Al

grain. In the bottom regions, Pb particles are generally more irregular in shape and less uniformly distributed among the pre-droplet boundaries. Some fine Pb particles were found within these boundaries. The lead distribution in the equiaxed region of alloy A111.5Si–15Pb is shown in Fig. 3. Lead distribution in the equiaxed region of the preforms suggests a strong liquid convection existed on the top surface of deposit during deposition stage. The equiaxed microstructure in the A1–Si–Pb alloys during LPCSF is believed to be a result of the following sequences. (i) Impingement of the droplet/powders experiencing various solidification conditions resulted in semi-solid slurry consisting mainly of A1–Si dendritic blocks surrounded by thin liquid films on the deposit surface. (ii) All lead in the slurry was in liquid state because the temperature of the deposit was much higher than the melting point of lead. The vigorous convection resulted in most of the liquid lead getting uniformly distributed in the liquid A1–Si alloy films. (iii) With A1–Si dendritic blocks growing, coarsening and liquid A1–Si alloy solidifying, the liquid lead particles were coalesced and pushed to the regions that finally formed grain boundaries. (iv) The Pb particles initially trapped in the solid powders and between the solid structure within semi-solid droplets were left in the A1 grain interiors.

Hot extrusion greatly reduces the grain size as well as porosity level of the preforms. But the microstructure is not uniform along the radial direction of the extruded rods due mainly to nonuniform deformation. The room-temperature tensile tests of the extruded A1–Si–Pb alloys show that they possess improved strengths and ductility compared to those fabricated by stir casting. The improvement in properties was attributed to the fine Si and Pb particle distribution in the nondendritic A1 matrix generated by LPCSF. The work-hardening rates of the test A1–Si–Pb alloys were found to be an order of magnitude lower than that of A1–Si alloys. The low work-hardening behavior due to the presence of lead particles prevents necking of the specimens. From SEM observation of the fracture surfaces, it was found that Pb particles act as void nucleation sites during test. The final failure is caused by the maximum shear stress lying in a plane oriented at 45° to the tensile axis by tearing off the thin links between the voids. Pb concentration was found to be a decisive factor controlling room-temperature tensile properties in these two leaded A1–Si alloys.

FIG 2. Optical micrograph showing exqiaxed structure in spray-formed LM6 alloy.

FIG. 3. SEM micrograph showing Pb alloy distribution in equiaxed region.

5. Conclusions

(1) Liquid-phase co-spray forming (LPCSF) has been successfully employed to fabricate Al–Si–Pb alloys at low pouring temperature. The fine equiaxed grain structure with uniform distribution of both fine Si and Pb particles in the matrix can be obtained by this technique. The alloys thus formed in the hot extruded condition possess improved room-temperature tensile property. Pb particles contribute to the low work-hardening behavior of this material and to void nucleation leading to fracture.

(2) LPCSF process shares the same principles with spray forming. The mechanisms responsible to microstructure formation in LPCSF process were understood based on the study of microstructural evolution during spray forming. It was found that the fundamental difference between spray forming and other semi-solid processing is on the solute concentration of the liquid films among the solid grains or dendritic blocks. It is this factor which results in fine equiaxed grain structure and low-solute segregation level.

(3) LPCSF process may be further applied to generate other difficult-to-make alloys or composites of new microstructure.

References

1. GRANT, P. S. — *Prog. Mater. Sci*, 1995, **39**, 497.
2. ENRIQUE, J. L — *Int. J. Rapid Solidification*, 1989, **5**, 47
3. ICHIKAWA, K. AND KINOSHITA, Y — *Mater. Trans. JIM*, 1993, **34**, 467.
4. WARD, P. J. *et al.* — *Acta Metall*, 1996, **44**, 1717.
5. PIERANTONI, M., GREMAUD, M., MAGNIN, P., STOLL, D. AND KURZ, W — *Acta Metall.*, 1992, **40**, 1637.
6. SURESH, A. AND DOHERTY, R. D. — *Int. J Powder Metall.*, 1993, **29**, 331.

Thesis Abstract (Ph. D.)

Fuzzy multiobjective models for water quality management of river systems by K. Sasikumar

Research supervisor: Prof. P. P. Mujumdar
Department: Civil Engineering

1. Introduction

Fuzzy multiobjective optimisation models are developed in the present study for water-quality management of river systems. Multiobjective models play a key role in arriving at best compromise solutions acceptable to both the pollution-control agency responsible for maintaining water quality of the river system and the dischargers disposing the pollutants into the river system. In general, the aspirations and interests of the pollution-control agency and dischargers are in conflict. Fuzzy decision making has been used as an effective tool for incorporating conflicting objectives in various management models for suggesting best compromise solutions.[1–3]

An attempt is made in this work to apply the concepts of fuzzy decision and fuzzy probability for developing multiobjective models for water-quality management of river systems. Three models, namely, fuzzy deterministic model, fuzzy probability model, and fuzzy seasonal model are developed in this study.

2. Model overview

Fuzzy deterministic model addresses the water-quality management of a river system in a deterministic framework. The model incorporates the conflicting objectives of the pollution-control agency and dischargers in the system. The vagueness associated with the setting up of the water-quality criteria, and the aspirations of the pollution-control agency and dischargers are quantified using fuzzy goals with appropriate membership functions. The membership functions of the fuzzy goals are viewed as functions representing the variation of satisfaction levels with regard to the attainment of their respective goals. Two formulations, namely, the MAX–MIN and MAX-BIAS formulations, are proposed for the fuzzy deterministic model. The MAX–MIN formulation maximizes the minimum satisfaction level in the system. The MAX–BIAS formulation maximizes a bias measure giving a solution that favours the dischargers. A salient feature of the model is the elimination of waste-treatment cost curves in the formulation. The model provides flexibility for the pollution-control agency and dischargers to specify their aspirations independently.

The fuzzy probability model addresses the uncertainty in a water-quality system in a fuzzy probability framework. Modelling of the uncertainty in a water-quality system may be made more versatile by incorporating vagueness together with randomness present in the system. The success of such a modelling effort lies in proper identification, description, and quantification of the events that are vaguely defined. Uncertainties due to both vagueness and randomness coexist in a river system. The occurrence of the event of low water quality is treated as a fuzzy event. The randomness associated with the water-quality index is then linked to this fuzzy event using the concept of probability of a fuzzy event. This linking essentially defines the risk of low water quality. In most of the existing water-quality management models, the risk level for violation of a water-quality standard is constrained by a pre-assigned value through a chance constraint. Instead of this, a range of risk levels is specified by considering a fuzzy set of low risk. Thus, two levels of uncertainty, one associated with low water quality and the other with low risk, are quantified and incorporated in the management model.

The fuzzy seasonal model takes into account the seasonal variations of river flow to specify the seasonal fraction removal levels for the pollutants. The seasonal variations in river flow cause varying assimilative capacities in the river system. For a river system with seasonal variation in river flow, different seasons are identified with a finite number of discrete water-quality states in each season. The seasonal variation of river flow is considered as a discrete-state stochastic process and is modelled as a first-order Markov chain. From the Markov chain model, the steady-state probability distributions of the water-quality states in all the seasons are computed. Fuzzy sets of low water quality are considered in each season. The membership functions of these fuzzy sets represent the degree of low water quality associated with the discrete states of water quality in a season. The fuzzy risk of low water quality in a season at a check point in the river system is expressed in terms of the degree of low water quality and the steady-state probabilities. The fuzzy risk forms the basis for the membership functions of the

fuzzy goals of the pollution-control agency. Considering the fuzzy goals of the pollution-control agency and dischargers, and the crisp constraints, the water-quality management problem is formulated as a fuzzy optimisation model. The solution of the model gives the seasonal fraction removal levels for the pollutants.

Applications of the three fuzzy multiobjective optimisation models are illustrated with hypothetical river systems. Linear and nonlinear programming techniques are used to obtain optimal solutions.

3. Conclusions

The cooperation between the pollution-control agency and dischargers, and the dischargers among themselves are made more realistic using the fuzzy multiobjective models. The models do not limit their applications to any particular pollutant or water-quality index in the river system. Given appropriate transfer functions for the spatial distribution of the pollutants in a river system, three fuzzy multiobjective models developed in this study may be used for water-quality management of the river system.

References

1 KINDLER, J. Rationalising water requirements with aid of fuzzy allocation model, *J. Wat. Res. Plann. Mgmt*, ASCE, 1992, **118**, 308–323.

2 LEE, Y W., DAHAB, M F. AND BOGARDI, I. Nitrate risk management under uncertainty, *J. Wat. Res. Plann. Mgmt*, ASCE, 1992, **118**, 151–165

3. CHANG, N. AND WANG, S W. Managerial fuzzy optimal planning for solid waste management systems, *J. Environ. Engng*, ASCE, 1996, **122**, 649–658.

Thesis Abstract (Ph. D.)

Development of robust higher order transverse deformable elements for composite laminates by P. Rama Mohan
Research supervisors: Profs T. S. Ramamurthy and B. Dattaguru
Department: Aerospace Engineering

1. Introduction

Laminated composites are fast replacing the conventional materials in aerospace industry and are often subjected to severe environmental conditions during their service life. Laminated structures that are very thick and/or highly flexible against transverse shear deformation demand accurate prediction of through-thickness distribution of both inplane and transverse stresses to find the possible failure locations. Analysis of anti-symmetric laminates requires proper representation of coupling between stretching and bending. Lo–Christensen–Wu (LCW) higher-order theory[1] provides a structural model, which has several advantages compared to classical or first-order theories in analysing the laminated structures. It allows quadratic variation of transverse shear strains and linear variation of transverse normal strain across

the thickness. It requires C^0-continuous description for the displacement components in finite-element formulations and hence is best suited for developing general-purpose finite-element packages. Because of these advantages, there is a demand for developing error-free, 1- and 2D finite elements based on LCW higher-order theory.

In the literature, no systematic studies are made to identify the problems of locking, stress oscillations, etc. in the case of C^0-continuous higher-order finite-element formulations. In this work, different issues involved in finite-element formulations based on LCW higher-order theory are critically examined when applied to two classes of structural problem, i.e. constrained elasticity media problems and structural problems with initial strains.

2. Variational formulations

It has been recognised that minimum total potential principle (MTPP) is inadequate to resolve the many challenges faced by C^0-continuous displacement-type finite-element formulations. In this work, different variational formulations based on LCW higher-order theory are discussed for analysing the laminated structures under hygrothermal environments. Variational, correctness requirements are obtained in a general sense using Hu–Washizu variational principle[2] which are required to reconstitute some of the strain/stress components in MTPP.

3. Constrained media elasticity

Shear flexible 2- and 3-noded higher-order beam elements, 4- and 9-noded higher-order plate elements are considered under the class of constrained media problems in which the transverse shear strain is constrained in the thin limits. In the case of higher-order beam elements, the discretized Cartesian transverse shear strains are expanded in terms of Legendre polynomials,[3] the cause for the errors of locking, delayed convergence and stress oscillations is located; consistent forms for discretized transverse shear strains are identified for both linear and quadratic elements. Variationally correct higher-order beam elements are designed by reconstituting the assumed transverse shear strain in the MTPP using field consistency and variational correctness requirements.

In the case of plate elements, it is difficult to identify spurious constraints by expanding the transverse shear strains explicitly in the Cartesian system. So, covariant base approach is adapted for plate-element formulations on certain principal lines, field inconsistencies which lead to spurious constraints in the penalty limits are identified; the consistent forms for covariant transverse shear strains are established. Variationally correct bilinear and biquadratic higher-order rectangular plate elements are designed by reconstituting the covariant transverse shear strains in accordance with field consistency and variational correctness requirements.

For a distorted element configuration, nonuniform mapping disturbs the consistency of transverse shear strains in the Cartesian system. General quadrilateral 4- and 9-noded higher-order plate elements are designed by mapping the consistent covariant pseudo shear strains from the natural coordinate system to the Cartesian system in a consistent manner. The method of nodal Jacobian transformation[4] is used for this purpose. These elements satisfy both field- and edge-consistency requirements and are therefore free of locking even when used in dis-

torted meshes. The robustness of field- and edge-consistent bilinear and biquadratic higher-order plate elements is demonstrated using several benchmark tests.

4. Structures with initial strains

Structures subjected to hygro-thermal loads being the best example of structures with initial strains are considered under this topic. Because of the similarity in the analysis of structures under thermal and moisture loads, thermal stress analysis is chosen for examining different issues involved in the C^0-continuous higher-order finite-element formulations.

A special beam element formulation is considered for analysing the problems associated with thermal stress analysis when the beam is subjected to varying temperatures along the mid-plane. It is found that conventional 2- and 3-noded higher-order beam elements suffer from both inaccurate displacement as well as inaccurate stress recovery unlike their first-order counterparts[5] which suffered from poor stress recovery only. It is argued here that the errors in the conventional elements are due to conflicting participation of higher-order terms of initial strain and transverse total normal strain fields in energy computation. A priori error models are derived for the inconsistent 2- and 3-noded beam elements and are verified using benchmark tests.

Consistent and variationally correct 2- and 3-noded beam elements are designed by consistently reconstituting the transverse total normal and initial strain fields to the order of inplane total strain field in accordance with the orthogonality conditions. It is demonstrated analytically and using finite-element method that consistent elements give variationally correct strain fields within the element domain exactly for all the problems. An interesting conflict between continuity and consistency requirements has been noticed in consistent element formulations.

Again, analytical a priori error models are derived for total strains in conventional finite-element formulations when temperature distribution across the thickness is not linear in nature and are verified using numerical examples. It is argued here that the errors in the original LCW model are due to conflicting participation of initial strain field components in forming different energy components in MTPP. Original LCW higher-order model is modified by relieving the conflict in initial strain participation in energy formation so that it can provide a cubic through-thickness accuracy for the inplane total strain/stress fields and a linear through-thickness accuracy for transverse total normal strain/steel field. A refined C^0-continuous higher-order model is proposed so that it can give uniform cubic through-thickness accuracy for both inplane and transverse normal total strain/stress components. The expected accuracy from the modified and refined models are a priori derived using simple variational techniques.

5. Applications

A general displacement-type finite-element procedure has been given for applications of higher-order plate elements to the static, buckling and free vibration analysis of laminated composite plates under hygrothermal environments. Interlaminar stresses across the laminate thickness are predicted using layer-wise equilibrium equations. Different classes of stability problems—estimations of critical buckling applied loads, critical buckling temperature, critical buckling moisture concentration, effect of temperature and moisture concentration on the criti-

cal buckling applied loads—which are very useful in the design and analysis of laminated structures are analysed. Natural frequencies of laminated anisotropic plates are estimated using consistent mass matrices. Results are compared with experimental and 3D elasticity solutions. Some parametric influences on the buckling strength and on the natural frequencies of rectangular laminated plates are critically examined. Robustness of field- and edge-consistent bilinear and biquadratic higher-order elements is demonstrated by solving a number of structural problems with mesh distortions.

6. Conclusions

Variationally accurate C^0-continuous finite elements based on LCW higher-order theory are developed using assumed strain displacement method for the analysis of laminated structures under hygrothermal environments. A number of new paradigms—constrained field consistency, variational correctness, consistent mapping, edge consistency and unconstrained field consistency—are respected in the formulations. Orthogonality conditions which are required for reconstituting the strain components in MTPP are obtained using Hu–Washizu variational principle.

References

1. Lo, K. H., Christensen, R. M. and Wu, E. M. — A higher order theory of plate deformation, part I. homogeneous and plates, *ASME J. Appl. Mech.*, 1977, **44**, 663–668.
2. Hu, H. C. — On some variational principles in the theory of elasticity and the theory of plasticity, *Sci. Sinica*, 1955, **4**, 33–54.
3. Naganarayana, B. P., Prathap, G., Dattaguru, B. and Ramamurthy, T. S. — A field-consistent and variationally correct representation of transverse shear strains in the nine-noded plate element, *Comput. Methods Appl. Mech. Engng*, 1992, **97**, 355–374.
4. Prathap, G. and Somashekar, B. R. — Field- and edge-consistency synthesis of a four-noded quadrilateral plate bending element, *Int. J. Numerical Methods Engng*, 1988, **26**, 1693–1708
5. Prathap, G. and Naganarayana, B. P. — Consistent thermal stress evaluation in finite elements, *Computers Struct.*, 1995, **54**, 415–426.